All-optical detection of the spin Hall angle in W/CoFeB/SiO_2 heterostructures with varying thickness of the tungsten layer

Sucheta Mondal, Samiran Choudhury, Neha Jha, Arnab Ganguly, Jaivardhan Sinha, and Anjan Barman*
Department of Condensed Matter Physics and Material Sciences, S. N. Bose National Centre for Basic Sciences, Block JD, Sec. III, Salt Lake, Kolkata 700106, India

(Received 9 February 2017; revised manuscript received 14 July 2017; published 10 August 2017)

The development of advanced spintronics devices hinges on the efficient generation and utilization of pure spin current. In materials with large spin-orbit coupling, the spin Hall effect may convert charge current to pure spin current, and a large conversion efficiency, which is quantified by spin Hall angle (SHA), is desirable for the realization of miniaturized and energy-efficient spintronic devices. Here, we report a giant SHA in beta-tungsten (β-W) thin films in Sub/W(t)/$Co_{20}Fe_{60}B_{20}$(3 nm)/SiO_2(2 nm) heterostructures with variable W thickness. We employed an all-optical time-resolved magneto-optical Kerr effect microscope for an unambiguous determination of SHA using the principle of modulation of Gilbert damping of the adjacent ferromagnetic layer by the spin-orbit torque from the W layer. A nonmonotonic variation of SHA with W layer thickness (t) is observed with a maximum of about 0.4 at about $t = 3$ nm, followed by a sudden reduction to a very low value at $t = 6$ nm. This variation of SHA with W thickness correlates well with the thickness-dependent structural phase transition and resistivity variation of W above the spin-diffusion length of W, while below this length the interfacial electronic effect at W/CoFeB influences the estimation of SHA.

DOI: 10.1103/PhysRevB.96.054414

I. INTRODUCTION

The exciting new frontier of spintronics [1,2] and magnonics [3,4] research is driven by the need of utilizing the spin-orbit (SO) effect for obtaining pure spin current [5,6]. An important aspect of improving the performance of the device is to minimize Joule heating, which requires fundamentally pure spin current [5–7]. It is quite nontrivial to generate and transport the spin current. Some of the earlier studies have used nonlocal spin-injection techniques [8–10], spin pumping [11–13], and the Rashba effect [14] for generating spin currents. Moreover, utilization of pure spin current for magnetization manipulation poses additional challenges. Recent finding of the spin Hall effect (SHE) [15] has opened up the possibility of utilizing pure spin current for manipulation of magnetic moments [5,16,17]. To quantify the SHE, an important parameter, namely, spin Hall angle (SHA), has been proposed and it is related to the conversion efficiency of charge-to-spin current [18,19]. Considerable efforts have been devoted to estimating and understanding the value of SHA for various heavy metals (HMs). Particularly, the SHE in HM layers can generate sufficiently large spin current to manipulate magnetic moments of a ferromagnetic layer adjacent to the HM layer as it exerts significant spin torque [16,20]. Furthermore, the SHE-induced spin-orbit torques (SOTs) have been shown to induce the large domain wall velocity [17], excite precessional magnetization dynamics [21–23], as well as result in magnetization switching [24]. Remarkably, it has been recently demonstrated that by using sophisticated device structuring, SOT-induced magnetization switching can be triggered in the absence of any magnetic field [25–27]. Some key requirements for technological implementation of the above-mentioned interesting applications are to search for HMs with reasonably large SHA, investigation of various factors affecting the SHA of HM thin films, and to understand the variation of SHA in such HM thin films by controlling those factors. An important issue in this research is to establish an accurate and unambiguous measurement technique of SHA. The precise quantification of SHA and its origin in a conventional metal-based system is of technological interest for spintronics-based device applications. In general, the techniques used for determining the SHA are the spin torque ferromagnetic resonance technique [16,28,29], spin torque switching of perpendicularly magnetized films [26], and measurement based on nonlocal spin valves [7]. All these techniques primarily rely on electrical excitation, detection, and extremely delicate microfabrication [30]. Recently, it has been demonstrated that by using the time-resolved magneto-optical Kerr effect (TRMOKE) [31] technique SHA can be measured more conveniently in a noninvasive manner without the requirement of advanced microfabrication and electrical detection, and more precise estimate of SHA may be obtained [32].

The highly resistive β-tungsten (distorted tetragonal phase commonly referred to as A15 structure) is known to be one of the efficient materials for exhibiting large SHA due to strong SO coupling [33]. Also, in ferromagnetic thin-film heterostructures, use of tungsten (W) leads to highly stable perpendicular magnetic anisotropy [34] and interfacial Dzyaloshinskii-Moriya interaction [35]. Another important characteristic associated with W is the thickness-dependent phase transition exhibited by it, usually observed in the thickness range of sub-10 nm [36,37]. In general, sputter-deposited W films with thickness below 5 nm are found to have β phase with resistivity larger than 150 $\mu\Omega$-cm, whereas the films with thickness above 5 nm possess predominantly α phase (bcc structure) with resistivity of about 40 $\mu\Omega$-cm [24,33,38]. To date, the SHA for W has been reported in few studies mostly in β phase. However, a systematic study of SHA in W/ferromagnet (FM)/oxide heterostructure with W layer thickness varying across the structural phase transition is

*abarman@bose.res.in

missing. Depending on the deposition condition, SHA values of up to about 0.4 have been reported specifically for β phase of W [24,39]. Few papers have mentioned relatively small SHA for α phase of W [33]. Therefore, it calls for investigating the systematic dependence of SHA on the structural phase of W which is intricately related to its thickness. Furthermore, few important recent studies have suggested that the transparency of HM/FM interface plays a crucial role in evaluating the SHA of HM layer [40–42]. Additionally, a theoretical study has classified the bulk and interface SHE and claimed that the interface SHE may be as large as 25 times the bulk SHE [43]. Recently, by alloying different HM layers, attempts have been made to achieve large SHA [44]. All these studies relate to the intricate role of spin-orbit coupling-induced SHE in generating pure spin current that is aimed toward utilization for device applications.

Here, we present the correlation between thickness-dependent phase transition in W thin films and large SHE-induced modulation of damping (MOD) in technologically important Sub/W(t)/$Co_{20}Fe_{60}B_{20}$(3 nm)/SiO_2(2 nm) heterostructures. The all-optical detection technique TRMOKE is used for investigating the magnetization dynamics [32]. Utilizing the sensitive variation of MOD, we estimate the SHA. We observe a clear variation in the value of estimated SHA with the phase of W underlayer. However, even within the β phase, when the thickness of W is smaller than its spin-diffusion length, the value of SHA is found to be significantly low. We correlate this variation of SHA with the SO coupling of the bulk of the HM layer as well as the interfacial electronic effect at the HM/FM interface.

II. SAMPLE PREPARATION AND CHARACTERIZATION

The thin-film heterostructures Sub/W(t)/$Co_{20}Fe_{60}B_{20}$(3 nm)/SiO_2(2 nm) with t = 2–7 nm in steps of 1 nm were deposited by dc/rf magnetron sputtering on Si (100) wafers coated with 100 nm SiO_2. The purpose of varying W underlayer thickness was to choose W thickness across the phase transition regime. The base pressure of the deposition chamber was better than 2×10^{-7} Torr. CoFeB and W were grown using dc power of 20 W, whereas the SiO_2 was grown using rf power of 60 W at 13.56 MHz. All thin films were grown in Ar gas atmosphere of 1-mTorr pressure and deposition conditions were carefully optimized [35]. Using a shadow mask, 5-nm-thick chromium/25-nm-thick gold contact electrodes were first prepared, followed by deposition of the sample stack of 3 mm × 1 mm dimension between the contact electrodes using another shadow mask. The dc charge current was applied along the length of the sample using a standard source meter (U3606A, Agilent Technologies) and experimental arrangement allowed us to suitably choose the applied bias magnetic field angle with respect to the current flow direction. Time-resolved magneto-optical Kerr effect microscopy was exploited to study the magnetization dynamics of the heterostructures. The second harmonic (wavelength: 400 nm, pulse width: 100 fs) of a mode-locked Ti-sapphire oscillator (Tsunami, Spectra Physics) was used as the pump beam to excite the magnetization dynamics in the samples, whereas the fundamental laser beam (wavelength: 800 nm, pulse width: 80 fs, repetition rate: 80 MHz) was used as the probe beam to detect polar Kerr rotation from the sample as a function of the time delay between the pump and the probe beam [31,32]. The temporal resolution of the measurement is limited by the cross-correlation between the pump and probe pulses. A large magnetic field is first applied at a small angle of about 15° to the sample plane to saturate its magnetization. This is followed by reduction of the magnetic field to the bias field value (H = in-plane component of the bias field), which ensures that the magnetization remains saturated along the bias field direction. The slight tilt of magnetization from the sample plane ensures a finite demagnetizing field along the direction of the pump pulse, which is further modified by the pump pulse to launch a precessional dynamics within the sample. In our experiment a 1.7 ns time window has been used, which gave a damped uniform precession of magnetization. The pump and probe beams are made collinear and are focused on the sample through a microscope objective with numerical aperture = 0.65. At the focal plane of the probe (diameter $\approx$ 800 nm) the pump beam is slightly defocused and has a larger diameter ($\approx$1 μm) than the probe beam. The probe beam is carefully centered on the pump beam so that the Kerr signal can be collected from the uniformly excited part of the sample and slight misalignment during the course of the experiment does not affect the pump-probe signals. The pump beam is chopped at 2-kHz frequency and the Kerr rotation in the reflected probe pulse is detected by using a balanced photodiode detector and lock-in amplifier in a phase-sensitive manner. The time-resolved reflectivity data are simultaneously recorded to ensure that there is no breakthrough of Kerr rotation and reflectivity data into one another. The pump and probe fluences are chosen to be about 10 and 2 mJ/cm^2, respectively, to avoid the transient increment in damping due to laser heating. All the experiments were performed under ambient condition. Atomic force microscope was used to investigate the surface topography, whereas vibrating sample magnetometer was used to characterize the static magnetic properties of these heterostructures. Using standard four-probe technique the resistivity of W film was determined and the grazing incidence x-ray diffraction was used for investigating the phase of W.

III. RESULTS AND DISCUSSION

Figure 1(a) shows the grazing incidence x-ray diffraction (XRD) patterns for Sub/W(t)/$Co_{20}Fe_{60}B_{20}$(3 nm)/SiO_2(2 nm). In these XRD plots, the peaks corresponding to α- and β phase of W are marked. The high-intensity XRD peak at ~40.5° corresponds primarily to the α phase (bcc structure) of W (~40.5°) (110) orientation. Interestingly, we find that the peak in the vicinity of 40.5° is present for all thicknesses of W, but when the W thickness is less than 6 nm, then the peaks (~34.8° and ~42.1°) corresponding to β-W (A15 structure) with (200) and (211) crystal orientations appear [38,41]. One may note that in close proximity to 40°, β-W peak for (210) crystal orientation could also be present, which is quite difficult to identify. We wish to clarify here that for W thickness below 5 nm the β-rich phase along with a small amount of α phase exists, while with increasing thickness of the W layer the fraction of the α phase increases and starts to dominate for W thickness above 5 nm. For the sake of simple notation we

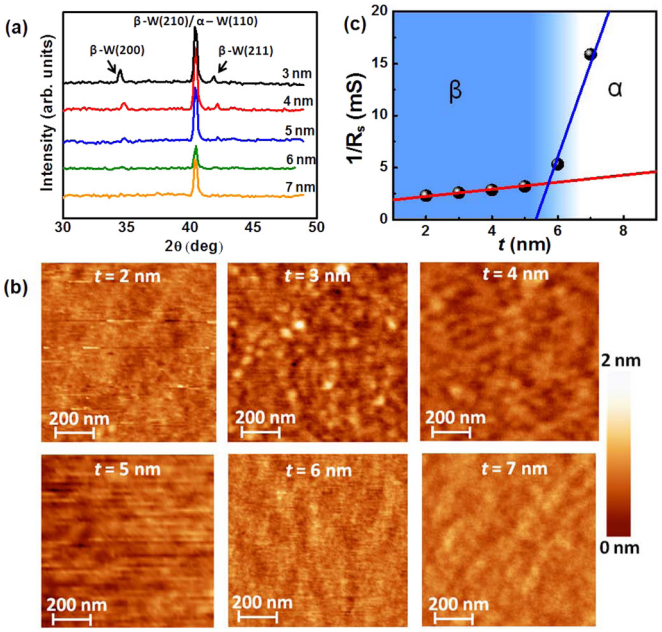

FIG. 1. (a) X-ray diffraction patterns measured at grazing angle incidence for W films with thickness of 3, 4, 5, 6, and 7 nm. Peaks corresponding to β- and α phase of W are marked in the plots. (b) Atomic force microscope images showing the surface topography of the Sub/W(t)/$Co_{20}Fe_{60}B_{20}$(3 nm)/SiO_2(2 nm) samples with $t = 2$–7 nm. The images are presented with the same scale bar as shown at the right-hand side of the figure. (c) Variation of inverse of sheet resistance of Sub/W(t)/$Co_{20}Fe_{60}B_{20}$(3 nm)/SiO_2(2 nm) as a function of W thickness (t) measured using linear four-probe technique.

refer to the phase below 5-nm W as β phase and above this thickness as α phase. These findings are consistent with some of the existing literature papers, where it is described that W exhibits a transition from β phase (A15 structure) to α phase (bcc structure) with increasing film thickness in the range of about 5 to 6 nm [36,37]. It has also been shown in some other studies that this transition thickness may be increased or decreased by carefully tuning the deposition conditions of the W thin films [38,45].

In Fig. 1(b), the atomic force microscope images for all the Sub/W(t)/$Co_{20}Fe_{60}B_{20}$(3 nm)/SiO_2(2 nm) heterostructures investigated in the present study are shown. We have used WSxM software to process the images [46]. From these images we obtained the average topographical roughness for the samples with $t = 2$, 3, 4, 5, 6, and 7 nm as listed below (Table I).

The roughness values vary by about 10% when measured at various regions of space of the same sample. Overall, the topographical roughness in all film stacks is found to be significantly small irrespective of whether the W thickness corresponds to its β- or α phase. Due to the small thicknesses of the thin-film heterostructures, presumably the interfacial roughness will clearly show its imprint on the topographical roughness. We thus infer that the interfacial roughness, if any, present in these heterostructures is very small and is similar in all samples.

TABLE I. Average roughness values obtained using atomic force microscopy for Sub/W(t)/$Co_{20}Fe_{60}B_{20}$(3 nm)/SiO_2(2 nm) samples with different W thicknesses.

W thickness (nm)	2	3	4	5	6	7
Average roughness (nm)	0.21	0.21	0.16	0.19	0.14	0.23

To determine the variation of resistivity of W with its thickness across the two different phases, we performed four-probe measurements on all the samples. Charge current was applied along the length of the sample and the experiment was performed in constant current mode [47]. The inverse of sheet resistance (R_s) of the film stack as a function of W thickness is plotted in Fig. 1(c). A change of the slope is observed beyond 5 nm, which indicates a change in the W resistivity. We estimate the average resistivity of W in β- and α-rich phase to be about 260 and 105 μΩ-cm, respectively.

A. Principle behind the determination of spin Hall angle

We next focus on the mechanism involved in the tuning of magnetization dynamics under the influence of spin current. Figures 2(a) and 2(b) show the schematics of experimental arrangement before and after the approach of pump-probe pulses. The flow of charge current through the W layer and consequent spin-current generation due to SHE are shown along x- and z directions, respectively. Under the influence of spin current, the CoFeB layer experiences an antidamping like SOT and the magnetization dynamics is governed by a modified Landau-Lifshitz-Gilbert equation [32] as given below:

$$\frac{d\hat{m}}{dt} = -\gamma(\hat{m} \times H_{\text{eff}}) + \alpha\left(\hat{m} \times \frac{d\hat{m}}{dt}\right) + \frac{\hbar}{2e\mu_0 M_s d} J_s(\hat{m} \times \hat{\sigma} \times \hat{m}). \quad (1)$$

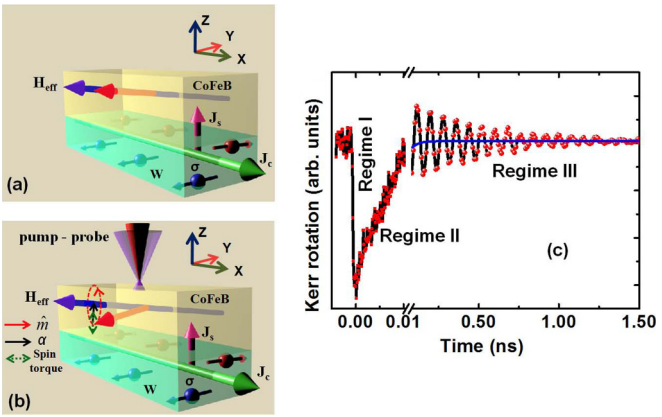

FIG. 2. Schematic of sample geometry and illustration of experimental geometry (a) before and (b) after the approach of pump and probe laser pulses. Coordinate convention as followed is also shown. The blue and red cylindrical arrows indicate the orientation of effective magnetic field and initial magnetization, respectively. (c) Time-resolved Kerr rotation data for Sub/W(4 nm)/$Co_{20}Fe_{60}B_{20}$(3 nm)/SiO_2(2 nm) sample at applied field $H = 1.46$ kOe are shown. The three different temporal regimes are indicated in the graph.

Here, γ is the gyromagnetic ratio, $\hat{\sigma}$ is the spin-polarization vector, $\hat{m}$ is the magnetization vector, M_s is saturation magnetization, J_s is spin-current density, H_{eff} is the effective magnetic field, d is the ferromagnetic layer thickness, and α is the Gilbert damping constant [7,48]. Depending on the polarity of $\hat{\sigma}$, the spin torque [28] acts collinearly against or toward the intrinsic Gilbert damping of the precessing magnetization. Effective damping, in turn, gets modulated depending on the injected spin-current density and relative orientation between the magnetic moment (which lies along the direction of magnetic field) and charge current density [28]. The modulation of damping under the influence of spin current [32] can be expressed as

$$\Delta\alpha = (\alpha_{\text{eff}} - \alpha_0) = \hbar\gamma J_s / 2eM_s d 2\pi f, \tag{2}$$

where α_0 and α_{eff} are the damping in the absence and presence of applied charge current, respectively, e is electronic charge, f is the precessional frequency, and other symbols have the same meaning as described before in the text. This approach is valid in the high-field limit and assuming that the magnetic moment and the direction of the charge current are perpendicular to each other [49,50]. Thus, the SHA (charge current to spin-current conversion efficiency) is given by

$$\theta_{\text{SH}} = \frac{J_s}{J_c} = 2eM_s d 2\pi f \Delta\alpha / \hbar\gamma J_c \sin\theta, \tag{3}$$

where charge current density through the W layer has been denoted as J_c. θ is the angle between J_c and bias magnetic field direction, which is 90° in the present case. Experimentally, we find the value of $\Delta\alpha/J_c$ and estimate the SHA using the above expression.

B. All-optical investigation of magnetization dynamics

In Fig. 2(c), the as-measured data using TRMOKE setup are shown for the Sub/W(4 nm)/$Co_{20}Fe_{60}B_{20}$(3 nm)/SiO_2(2 nm) sample at $H = 1.46$ kOe without any applied charge current. The femtosecond laser excites the sample, thereby triggering the magnetization dynamics. Overall, the dynamics can be divided into three different temporal regimes as shown in the plot. Regime I (sharp drop immediately after negative delay, ~700 fs) corresponds to ultrafast demagnetization [51] and regime II corresponds to the fast relaxation (1.7 ps) due to the spin-lattice relaxation. Subsequently, in regime III, we observe a slower relaxation (~40 ps) along with magnetization precession, which gets damped in few ns. The slower relaxation is due to heat diffusion from the lattice to the substrate and surrounding. We mainly concentrate on regime III to estimate the damping and its modulation due to the action of spin torque. The blue line in Fig. 2(c) corresponds to the biexponential background present in the precessional data in regime III. We subtract this background from the raw data and fit the resulting data using standard damped harmonic function. From the fit we estimate the damping α_{eff} using the expression $\alpha_{\text{eff}} = 1/2\pi f\tau$, where f is the precessional frequency and τ is the relaxation time corresponding to magnetization oscillation.

We further studied the bias-field-dependent magnetization dynamics; Fig. 3(a) shows representative experimental data of precessional magnetization dynamics along with the theoretical fit using a damped sinusoidal function for Sub/W(4 nm)/$Co_{20}Fe_{60}B_{20}$(3 nm)/SiO_2(2 nm) sample. From the fitting, we extract the relaxation time (τ) as 0.52, 0.59, and 0.70 ns for bias field values of 1.46, 1.05, and 0.65 kOe, respectively. Figure 3(b) shows the corresponding fast Fourier transform (FFT, power vs frequency), from which the precessional mode frequency is extracted. The frequency (f) vs bias magnetic field (H) is plotted in Fig. 3(c) for the same film stack. The standard Kittel expression mentioned below is used to fit the f vs H data:

$$f = \frac{\gamma}{2\pi}[H(H + 4\pi M_{\text{eff}})]^{\frac{1}{2}}, \tag{4}$$

where $\gamma = g\mu_B/\hbar$, g is the Landé g factor, H is the applied bias magnetic field, and M_{eff} is the effective magnetization. From the fit M_{eff} and g are determined as fitting parameters. For these film stacks we obtain $M_{\text{eff}} \sim 1000 \pm 30$ emu/cc

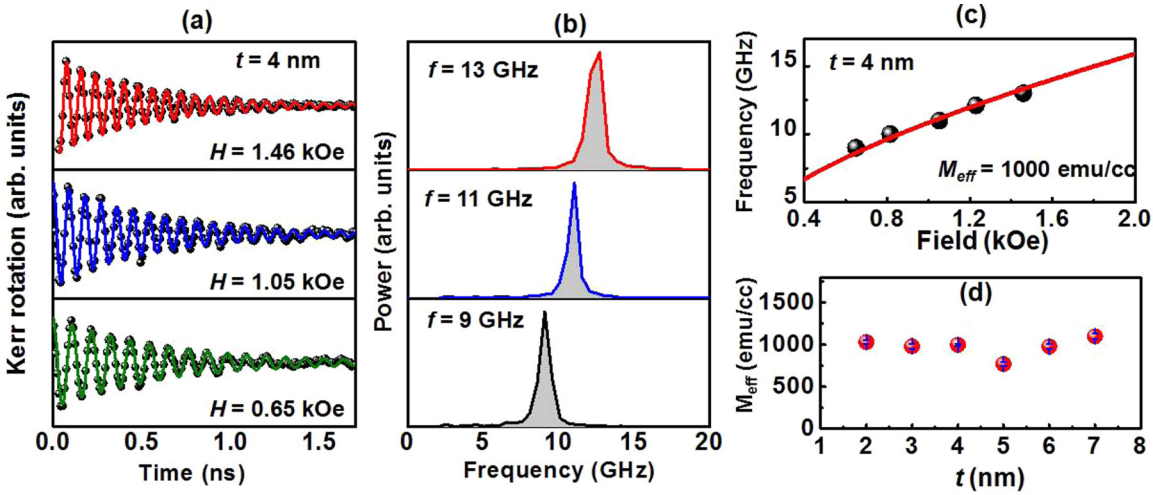

FIG. 3. (a) Time-resolved precessional magnetization dynamics for Sub/W(4 nm)/$Co_{20}Fe_{60}B_{20}$(3 nm)/SiO_2(2 nm) sample at different bias magnetic field values. (b) The corresponding FFT power spectra to extract the precession frequency. (c) Plot of variation of frequency as a function of bias magnetic field. The solid line is the fit with Kittel formula. (d) Saturation magnetization of the Sub/W(t)/$Co_{20}Fe_{60}B_{20}$(3 nm)/SiO_2(2 nm) samples as a function of W layer thickness.

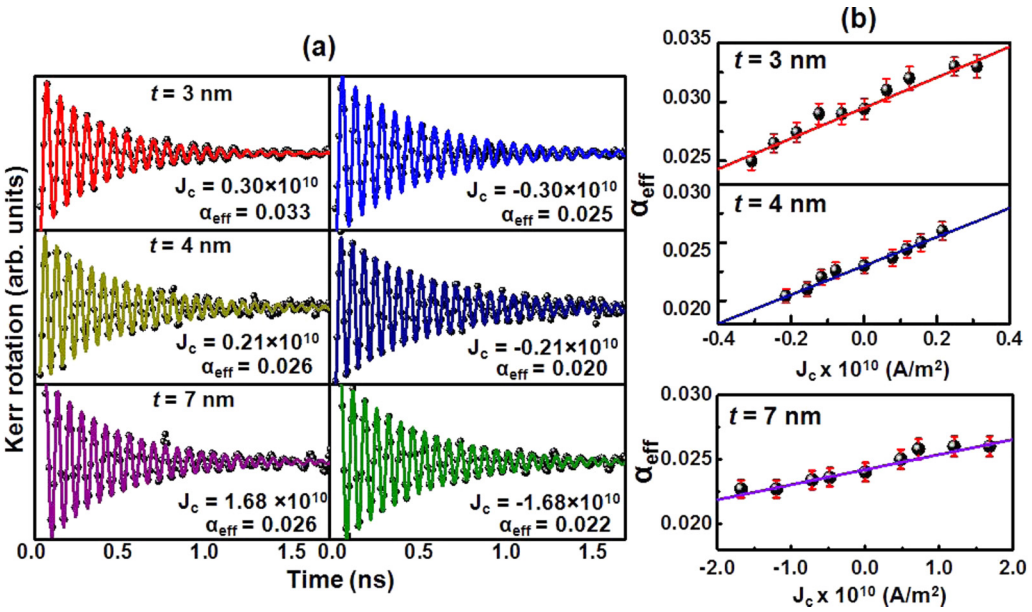

FIG. 4. (a) Representative TRMOKE traces for extraction of damping under the influence of positive and negative current densities. Here, W thickness is mentioned in the left panel. The estimated damping values at mentioned current densities (in A/m^2) are also shown. Comparison of left and right panels indicates that the damping value changes with the polarity of charge current. (b) Modulation of damping plot for W thickness of 3 and 4 nm corresponding to the β phase and 7 nm corresponding to the α phase. Solid line is the linear fit to the modulation of damping with current density. Error bars correspond to the fitting error obtained during the estimation of damping.

and $g = 2.0 \pm 0.05$, except for the W thickness of 5 nm, where M_{eff} is found to be lower (770 ± 24 emu/cc). In Fig. 3(d), the M_{eff} obtained from the dynamic measurement is plotted as a function of W thickness, t. Interestingly, for all the film stacks investigated in this study, M_{eff} is found to be close to the saturation magnetization M_s obtained using vibrating sample magnetometer. From this we infer that interface anisotropy is negligibly small in these heterostructures [35].

C. Spin-current-induced modulation of damping

Figure 4 shows some typical time-resolved Kerr rotation data after the application of dc charge current through the film stack with different polarities and the MOD as a function of the dc charge current density. The applied charge current through the heterostructure gets distributed into W and CoFeB layers according to the resistivity of each metallic layer. Here, J_c represents the current density through the W underlayer. Figure 4(a) shows the magnetization precession data at a bias field $H = 1.46$ kOe and for positive and negative $J_c(\theta = 90^\circ)$ along with the fit using damped sine function to extract the damping. The magnitude and sign of J_c and the corresponding extracted value of effective damping α_{eff} are mentioned in each panel. A direct comparison of MOD with applied J_c is shown for three representative thicknesses of W in Fig. 4(b), i.e. $t = 3$ nm, 4 nm (corresponding to β-rich phase), and 7 nm (corresponding to α-rich phase). From these plots, it is evident that the spin-current-induced spin torque generated by SHE almost linearly modulates the damping, consistent with the existing literature [28,32]. We use a linear fit and extract the slope of MOD ($\Delta\alpha/J_c$) in order to estimate the SHA using Eq. (3) for a given thickness of W. The values of the slope extracted from the fit for 2-, 3-, 4-, 5-, 6-, and 7-nm-thick W are tabulated below (Table II).

Note that the slope of MOD due to the spin current generated by SHE is generally larger for the β phase W (3, 4, 5 nm) in comparison to the α phase W (6, 7 nm). The sample with 2-nm W thickness is an exception and it will be discussed later in this paper. With increasing current density, precessional frequency has experienced a downshift for either direction of the charge flow [47]. This may possibly arise either from the Joule heating affecting the local magnetization as well as the frequency [32,47] or due to the presence of a fieldlike torque. The limited J_c value for the high resistive β-phase W [in Fig. 4(b), for $t = 3$ and 4 nm] is retained to avoid Joule heating in these films. Nevertheless, damping variation in α_{eff} up to $\pm 15\%$ is observed for a reasonably small current density of 0.3×10^{10} A/m^2 for the sample with $t = 3$ nm. Here we cannot rule out the possibility of small increment in damping values due to heat accumulation following the ultrafast demagnetization by the pump pulse on short time scales but that will not affect the slope of modulation of

TABLE II. Experimentally obtained values of modulation of damping for Sub/W(t)/$Co_{20}Fe_{60}B_{20}$(3 nm)/SiO_2(2 nm) samples with different W thicknesses.

W thickness (nm)	Modulation of damping (m^2/A)
2	$(0.47 \pm 0.04)\times10^{-12}$
3	$(1.29 \pm 0.10)\times10^{-12}$
4	$(1.20 \pm 0.06)\times10^{-12}$
5	$(1.02 \pm 0.04)\times10^{-12}$
6	$(0.39 \pm 0.06)\times10^{-12}$
7	$(0.11 \pm 0.01)\times10^{-12}$

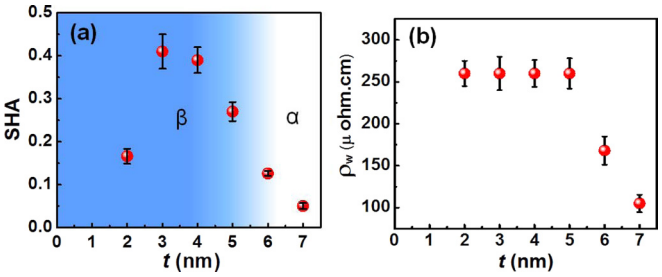

FIG. 5. (a) Variation of spin Hall angle with W thickness. Error bars are estimated by considering errors in damping, saturation magnetization, and resistivity measurements. The color contrast shows the transition from β- to α phase of W. (b) Variation of resistivity of W with thickness (t).

damping originating due to spin current generated by SHE. The enhancement (if any) will be constant and additive for all the represented damping values.

D. Tungsten layer thickness dependence of spin Hall angle

Figure 5(a) shows the plot of SHA as a function of W thickness $2\,\text{nm} \leqslant t \leqslant 7\,\text{nm}$ in Sub/W(t)/$Co_{20}Fe_{60}B_{20}$(3 nm)/SiO_2(2 nm). Interestingly, in this plot we notice that the SHA is quite small when the W layer thickness is 2 nm; subsequently, SHA increases to a large value for W layer thickness of 3 and 4 nm. For $t > 4\,\text{nm}$, the SHA decreases monotonically up to $t = 7\,\text{nm}$. It is important to emphasize here that we observe a giant value of SHA as large as 0.4 ± 0.04 for $t = 3\,\text{nm}$. Within the β phase of W, the SHA decreases as the thickness of W becomes comparable to spin-diffusion length of W (λ_{sf}) [45,52]. The observed dependence of SHA on W thickness from 2 to 4 nm can be explained by considering drift-diffusion analysis of the spin flow that incorporates spin Hall effect. Earlier theoretical and experimental studies have proposed that within the spin-diffusion length, the counter-flowing spin current generated due to vertical gradient in the spin-dependent electron chemical potential adjacent to the HM surface (under the assumption that no spin current penetrates out of HM) cancels the spin-Hall-generated spin current [24,45,50,53,54]. Due to this, the magnitude of the spin Hall spin current reduces significantly (resulting in smaller MOD and underestimation of SHA) as the thickness of the HM layer becomes comparable to λ_{sf}. From our experimental data we understand that the λ_{sf} of our W thin film is less than 3 nm as it is difficult to extract this parameter precisely using standard fit with few numbers of data points available in β-W phase. In order to understand whether the variation of SHA is directly correlated with the variation of resistivity, we plot the W resistivity with its thickness in Fig. 5(b). The significant drop in the resistivity value for $t > 5\,\text{nm}$ indicates a transition from β-W to α-W phase in the W film used in our experiment. It is important to notice here that the variation in SHA above spin-diffusion length is primarily correlated with the thickness-dependent β- to α-phase transition [structural change which is also related to the resistivity change; cf. Fig. 5(b)] of W [24,33,36,38,52]. Although from Fig. 5(b) the resistivity of 5-nm-thick W film is found to be primarily in β phase, from the trend of SHA values it appears that there is probably a mixed β- and α phase of W at this thickness. Hence, apart from W thickness of 2 and 5 nm, SHA is found to be in direct correspondence with the resistivity, which is similar to the variation of SHA with conductivity as observed for other HMs [44,55].

In the phase-transition regime, the change in crystal structure indicates a change in SO coupling strength of W which may play an important role in modifying the SHA [36]. There is a possibility that in the low resistive regime (for $t > 5\,\text{nm}$) the SHA is influenced by the change in SO coupling strength. As the phase transition in W with its thickness and the associated resistivity change predominantly originates from the bulk portion of W, thus it indicates that the bulk part of W plays a dominant role in defining the SHA and thereby the spin current above the spin-diffusion length of W. The bulk SHA in the HM layers is theoretically predicted and experimentally found to consist of contributions from the intrinsic, side-jump, and skew-scattering mechanisms [5,6,56]. SHA of W obtained in our experiment qualitatively follows the resistivity of the W layer, which indicates that the intrinsic or side-jump mechanism is primarily responsible for conversion of charge current to spin current [55]. However, it requires more elaborate study for full understanding of this phenomenon. The estimated large value of SHA indicates that the W/CoFeB interface is transparent enough to efficiently exert spin torque on the adjacent FM layer. The trend found in the variation of SHA with W thickness (β-W has larger SHA in comparison to α-W) is mostly consistent with earlier reported results [33], while the values of SHA obtained using all-optical detection technique are a new addition in this field. The method employed here is noninvasive and more unambiguous as it helps to eliminate any experimental artifacts involved in the electrical detection schemes [57]. Being a local technique, the all-optical method does not suffer from the large area averaging, which could have produced spurious effects due to inhomogeneities and defects present in the sample. Further, in the time-domain measurement technique, magnetization damping can be directly extracted from time-resolved precession data, which is more advantageous than other techniques such as FMR linewidth measurement, where excitation of multiple modes may lead to inhomogeneous line broadening, which could artificially increase the damping.

IV. CONCLUSION

In summary, we have used all-optical time-resolved magneto-optical Kerr effect microscopy to investigate the magnetization dynamics in Sub/W(t)/$Co_{20}Fe_{60}B_{20}$(3 nm)/SiO_2(2 nm) with varying W layer thickness under the influence of spin current generated by SHE. The W layer thickness is so chosen that it undergoes a transition from β-rich to α-rich phase at a thickness above 5 nm. For highly resistive β-phase W, large modulation of damping of up to $\pm 15\%$ at a modest current density of $0.3 \times 10^{10}\,\text{A/m}^2$ and corresponding SHA as large as 0.4 are achieved. The SHA above the spin-diffusion length of W follows the thickness-dependent phase transition of W. On the other hand, a smaller modulation of damping and underestimation of SHA is observed for W layer thickness smaller than its spin-diffusion length. In order to realize the

full value of spin current due to SHE, it is thus important to use the HM thickness above its spin-diffusion length. The variation of SHA with W thickness (β-W has larger SHA in comparison to α-W) is mostly consistent with the change in resistivity. Although in some of the recent theoretical and experimental studies direct correspondence of SHA with conductivity has been discussed, however we believe our investigations will trigger more studies to get further deep insight into the relationship between conductivity and spin Hall angle specifically for materials with mixed phase. Our results of detailed variation of SHA for different values of W thickness will be beneficial for in-depth understanding of correlation between the thickness-dependent phase transition in W and SHA. Furthermore, these studies will be significantly important from the application perspective as the future spintronic devices are expected to use large SHA material and spin-current-induced magnetization switching.

ACKNOWLEDGMENTS

We gratefully acknowledge the support from S. Pal in sample characterization. We acknowledge the financial assistance from the Department of Science and Technology Government of India under Grant No. SR/NM/NS-09/2011 and the S. N. Bose National Centre for Basic Sciences under Project No. SNB/AB/12-13/96. S.M. acknowledges DST under the INSPIRE scheme and S.C. acknowledges support from the S. N. Bose National Centre for Basic Sciences.

[1] A. Hoffmann and S. D. Bader, Phys. Rev. Appl. **4**, 047001 (2015).
[2] A. V. Chumak, V. I. Vasyuchka, A. A. Serga, and B. Hillebrands, Nat. Phys. **11**, 453 (2015).
[3] S. Neusser and D. Grundler, Adv. Mater. **21**, 2927 (2009).
[4] S. Choudhury, S. Saha, R. Mandal, S. Barman, Y. Otani, and A. Barman, ACS Appl. Mater. Interfaces **8**, 18339 (2016).
[5] A. Hoffmann, IEEE Trans. Magn. **49**, 5172 (2013).
[6] J. Sinova, S. O. Valenzuela, J. Wunderlich, C. H. Back, and T. Jungwirth, Rev. Mod. Phys. **87**, 1213 (2015).
[7] Y. Niimi and Y. Otani, Rep. Prog. Phys. **78**, 124501 (2015).
[8] Y. Fukuma, L. Wang, H. Idzuchi, S. Takahashi, S. Maekawa, and Y. Otani, Nat. Mater. **10**, 527 (2011).
[9] H. Idzuchi, Y. Fukuma, and Y. Otani, Sci. Rep. **2**, 628 (2012).
[10] V. E. Demidov, S. Urazhdin, R. Liu, B. Divinskiy, A. Telegin, and S. O. Demokritov, Nat. Commun. **7**, 10446 (2016).
[11] H. J. Jiao and G. E. W. Bauer, Phys. Rev. Lett. **110**, 217602 (2013).
[12] S. Maekawa, H. Adachi, K. Uchida, J. Ieda, and E. Saitoh, J. Phys. Soc. Jpn. **82**, 102002 (2013).
[13] M. Jamali, J. S. Lee, J. S. Jeong, F. Mahfouzi, Y. Lv, Z. Y. Zhao, B. K. Nikolic, K. A. Mkhoyan, N. Samarth, and J. P. Wang, Nano Lett. **15**, 7126 (2015).
[14] I. Mihai Miron, G. Gaudin, S. Auffret, B. Rodmacq, A. Schuhl, S. Pizzini, J. Vogel, and P. Gambardella, Nat. Mater. **9**, 230 (2010).
[15] J. E. Hirsch, Phys. Rev. Lett. **83**, 1834 (1999).
[16] L. Liu, C.-F. Pai, Y. Li, H. W. Tseng, D. C. Ralph, and R. A. Buhrman, Science **336**, 555 (2012).
[17] S. Emori, U. Bauer, S.-M. Ahn, E. Martinez, and G. S. D. Beach, Nat. Mater. **12**, 611 (2013).
[18] M. Morota, Y. Niimi, K. Ohnishi, D. H. Wei, T. Tanaka, H. Kontani, T. Kimura, and Y. Otani, Phys. Rev. B **83**, 174405 (2011).
[19] O. Mosendz, J. E. Pearson, F. Y. Fradin, G. E. W. Bauer, S. D. Bader, and A. Hoffmann, Phys. Rev. Lett. **104**, 046601 (2010).
[20] J. Kim, J. Sinha, M. Hayashi, M. Yamanouchi, S. Fukami, T. Suzuki, S. Mitani, and H. Ohno, Nat. Mater. **12**, 240 (2013).
[21] L. Liu, C.-F. Pai, D. C. Ralph, and R. A. Buhrman, Phys. Rev. Lett. **109**, 186602 (2012).
[22] M. Jamali, A. Klemm, and J.-P. Wang, Appl. Phys. Lett. **103**, 252409 (2013).
[23] M. Evelt, V. E. Demidov, V. Bessonov, S. O. Demokritov, J. L. Prieto, M. Muñoz, J. B. Youssef, V. V. Naletov, G. de Loubens, O. Klein, M. Collet, K. Garcia-Hernandez, P. Bortolotti, V. Cros, and A. Anane, Appl. Phys. Lett. **108**, 172406 (2016).
[24] Q. Hao and G. Xiao, Phys. Rev. Appl. **3**, 034009 (2015).
[25] D. Bhowmik, L. You, and S. Salahuddin, Nat. Nanotechnol. **9**, 59 (2014).
[26] J. Torrejon, F. Garcia-Sanchez, T. Taniguchi, J. Sinha, S. Mitani, J. V. Kim, and M. Hayashi, Phys. Rev. B **91**, 214434 (2015).
[27] G. Q. Yu, P. Upadhyaya, Y. B. Fan, J. G. Alzate, W. J. Jiang, K. L. Wong, S. Takei, S. A. Bender, L. T. Chang, Y. Jiang, M. R. Lang, J. S. Tang, Y. Wang, Y. Tserkovnyak, P. K. Amiri, and K. L. Wang, Nat. Nanotechnol. **9**, 548 (2014).
[28] S. Kasai, K. Kondou, H. Sukegawa, S. Mitani, K. Tsukagoshi, and Y. Otani, Appl. Phys. Lett. **104**, 092408 (2014).
[29] A. Ganguly, K. Kondou, H. Sukegawa, S. Mitani, S. Kasai, Y. Niimi, Y. Otani, and A. Barman, Appl. Phys. Lett. **104**, 072405 (2014).
[30] V. T. Pham, L. Vila, G. Zahnd, A. Marty, W. Savero-Torres, M. Jamet, and J. P. Attane, Nano Lett. **16**, 6755 (2016).
[31] A. Barman and A. Haldar, Solid State Phys. **65**, 1 (2014).
[32] A. Ganguly, R. M. Rowan-Robinson, A. Haldar, S. Jaiswal, J. Sinha, A. T. Hindmarch, D. A. Atkinson, and A. Barman, Appl. Phys. Lett. **105**, 112409 (2014).
[33] C.-F. Pai, L. Liu, Y. Li, H. W. Tseng, D. C. Ralph, and R. A. Buhrman, Appl. Phys. Lett. **101**, 122404 (2012).
[34] G. G. An, J. B. Lee, S. M. Yang, J. H. Kim, W. S. Chung, and J. P. Hong, Acta Mater. **87**, 259 (2015).
[35] A. K. Chaurasiya, C. Banerjee, S. Pan, S. Sahoo, S. Choudhury, J. Sinha, and A. Barman, Sci. Rep. **6**, 32592 (2016).
[36] J. Liu, T. Ohkubo, S. Mitani, K. Hono, and M. Hayashi, Appl. Phys. Lett. **107**, 232408 (2015).
[37] J. Torrejon, J. Kim, J. Sinha, S. Mitani, M. Hayashi, M. Yamanouchi, and H. Ohno, Nat. Commun. **5**, 4655 (2014).
[38] Q. Hao, W. Chen, and G. Xiao, Appl. Phys. Lett. **106**, 182403 (2015).
[39] C. Zhang, S. Fukami, K. Watanabe, A. Ohkawara, S. DuttaGupta, H. Sato, F. Matsukura, and H. Ohno, Appl. Phys. Lett. **109**, 192405 (2016).
[40] W. F. Zhang, W. Han, X. Jiang, S. H. Yang, and S. S. P. Parkin, Nat. Phys. **11**, 496 (2015).

[41] K. U. Demasius, T. Phung, W. F. Zhang, B. P. Hughes, S. H. Yang, A. Kellock, W. Han, A. Pushp, and S. S. P. Parkin, Nat. Commun. **7**, 10644 (2016).
[42] C. F. Pai, Y. X. Ou, L. H. Vilela-Leao, D. C. Ralph, and R. A. Buhrman, Phys. Rev. B **92**, 064426 (2015).
[43] L. Wang, R. J. H. Wesselink, Y. Liu, Z. Yuan, K. Xia, and P. J. Kelly, Phys. Rev. Lett. **116**, 196602 (2016).
[44] M. Obstbaum, M. Decker, A. K. Greitner, M. Haertinger, T. N. G. Meier, M. Kronseder, K. Chadova, S. Wimmer, D. Ködderitzsch, H. Ebert, and C. H. Back, Phys. Rev. Lett. **117**, 167204 (2016).
[45] J. W. Yu, X. P. Qiu, W. Legrand, and H. Yang, Appl. Phys. Lett. **109**, 042403 (2016).
[46] I. Horcas, R. Fernández, J. M. Gómez-Rodríguez, J. Colchero, J. Gómez-Herrero, and A. M. Baro, Rev. Sci. Instrum. **78**, 013705 (2007).
[47] See Supplemental Material at http://link.aps.org/supplemental/10.1103/PhysRevB.96.054414 for resistivity calculations and the investigation of the effect of Joule heating on the magnetization dynamics of the samples.
[48] L. Liu, T. Moriyama, D. C. Ralph, and R. A. Buhrman, Phys. Rev. Lett. **106**, 036601 (2011).
[49] K. Ando, S. Takahashi, K. Harii, K. Sasage, J. Ieda, S. Maekawa, and E. Saitoh, Phys. Rev. Lett. **101**, 036601 (2008).
[50] L. Liu, R. A. Buhrman, and D. C. Ralph, arXiv:1111.3702.
[51] E. Beaurepaire, J. C. Merle, A. Daunois, and J. Y. Bigot, Phys. Rev. Lett. **76**, 4250 (1996).
[52] S. Cho, S. H. C. Baek, K. D. Lee, Y. Jo, and B. G. Park, Sci. Rep. **5**, 14668 (2015).
[53] P. C. van Son, H. van Kempen, and P. Wyder, Phys. Rev. Lett. **58**, 2271 (1987).
[54] M. H. Nguyen, D. C. Ralph, and R. A. Buhrman, Phys. Rev. Lett. **116**, 126601 (2016).
[55] E. Sagasta, Y. Omori, M. Isasa, M. Gradhand, L. E. Hueso, Y. Niimi, Y. Otani, and F. Casanova, Phys. Rev. B **94**, 060412(R) (2016).
[56] X. Zhou, M. Tang, X. L. Fan, X. P. Qiu, and S. M. Zhou, Phys. Rev. B **94**, 144427 (2016).
[57] I. Neudecker, G. Woltersdorf, B. Heinrich, T. Okuno, G. Gubbiotti, and C. H. Back, J. Magn. Magn. Mater. **307**, 148 (2006).